A fast cardiac electromechanics model coupling the Eikonal and the nonlinear mechanics equations

Simone Stella

MOX, Dipartimento di Matematica
Politecnico di Milano, Milan, Italy
simone.stella@polimi.it

Francesco Regazzoni*

MOX, Dipartimento di Matematica
Politecnico di Milano, Milan, Italy
francesco.regazzoni@polimi.it

Christian Vergara

LABS, Dipartimento di Chimica, Materiali e Ingegneria Chimica "Giulio Natta"
Politecnico di Milano, Milan, Italy
christian.vergara@polimi.it

Luca Dedè

MOX, Dipartimento di Matematica
Politecnico di Milano, Milan, Italy
luca.dede@polimi.it

Alfio Quarteroni

MOX, Dipartimento di Matematica
Politecnico di Milano, Milan, Italy
Institute of Mathematics
École Polytechnique Fédérale de Lausanne, Switzerland
alfio.quarteroni@polimi.it

We present a new model of human cardiac electromechanics for the left ventricle where electrophysiology is described by a Reaction-Eikonal model and which enables an off-line resolution of the reaction model, thus entailing a big saving of computational time. Subcellular dynamics is coupled with a model of tissue mechanics, which is in turn coupled with a windkessel model for blood circulation. Our numerical results show that the proposed model is able to provide a physiological response to changes in certain variables (end-diastolic volume, total peripheral resistance, contractility). We also show that our model is able to reproduce with high accuracy (and with a considerably lower computational time) the results that we would obtain if the monodomain model should

*Corresponding author.

be used in place of the Eikonal model.

Keywords: Cardiac electromechanics, Eikonal model, PV loops, Numerical simulations.

AMS Subject Classification: 22E46, 53C35, 57S20

Please cite as: Simone Stella, Francesco Regazzoni, Christian Vergara, Luca Dedé and Alfio Quarteroni, A fast cardiac electromechanics model coupling the Eikonal and the nonlinear mechanics equations, *Mathematical Models and Methods in Applied Sciences* Vol. 32, No. 08, pp. 1531-1556 (2022)
`https://doi.org/10.1142/S021820252250035X`

1. Introduction

The functioning of the heart is driven by three main physical processes: electrophysiology, tissue mechanics and blood dynamics. Electrophysiology drives the mechanical wall deformation through the propagation of an action potential that stimulates cardiomyocites to contract, thanks to the generation of active forces.

The electrophysiology (EP) of the heart is often modeled by either the *bidomain* or the *monodomain* model,[22,45,46,57] time-dependent nonlinear PDEs describing the electrical activity of the myocardium in terms of variations of transmembrane potential coupled with a system of ODEs for the ionic currents. Both models accurately describe the EP of the myocardium;[21,45,64] However, due to the small space and time discretization parameters needed to capture the propagating front,[39,44] such models are so computationally demanding to harm their interest in the clinical practice.

To accurately describe the heart function, EP models should be coupled with models for the active force generation and active/passive mechanics.[35,46] The active force generation can be described by phenomenological models,[33,38] by approximations of physics-based models,[29,52,68] or by fully physics-based models,[29,49,50,68] which derive force generation models from the first physics principles.

The coupling of cardiac electromechanics (EM) models with blood circulation is often obtained by the simple windkessel or closed-loop lumped parameter models.[7,11,27]

All these mathematical models, which describe different physical processes, interact one another, leading to a highly coupled system.[3,6,16,54,58,60] Computational strategies for the resulting cardiac EM models have made significant developments in recent years.[3,12,28,33,62] However, as mentioned above for EP models, the computational costs typically remain still very large.

To overcome such limitations, in Ref. 61 the authors proposed to use a reduced EP model, namely the *Reaction-Eikonal* (RE) model,[37] in the context of an EM description. The RE model is an extension of the *Eikonal* model,[19,20,22,46] the latter being a steady problem describing the activation times, widely used thanks

to its very low computational costs.[13,32,41] In particular, the RE model consists in exploiting the solution of the Eikonal problem for the computation of the applied current to be used in an unsteady monodomain-like reaction problem. The latter is numerically approximated following the Finite Element Method on the Eikonal mesh, a coarser mesh with respect to the fine one needed by mono- and bidomain models, allowing to obtain the transmembrane potential and the ionic variables. With respect to standard numerical strategies for EM, the idea in Ref. 61 allows to simplify the EP step, as it requires to solve at each time step a reaction problem on a coarse mesh, see also Ref. 62.

The main goal of the present paper is to improve the strategy proposed in Ref. 61 by further reducing the computational burden. Moreover, while the analysis carried out in Ref. 37 focused on electrophysiological outputs, in this paper we investigate the ability of an EM model based on a RE-like model to faithfully reproduce mechanical outputs (such as pressure-volume loops), with an accuracy comparable with that achievable using the full monodomain model. The aim is to test whether the lack of mechano-electrical feedbacks, which the Eikonal model neglects by construction, can affect the quality of the results. In particular, the novelties of the paper consist in: (i) the proposal of an efficient way to solve the reaction problem, based on pre-computed solutions, shifted in time according to the solution of the Eikonal equation; (ii) the coupling of the EP with a physics-based active force model (RDQ20-MF),[50] which can provide mechanistic understanding, unlike phenomenological models. (iii) an analysis of numerical results, reproducing significant mechanical outputs such as PV loops and ejection fraction; (iv) a comparison of the mechanical outputs in EM obtained describing EP either through the monodomain or the RE model.

The structure of this paper is as follows. In Sec. 2, we present the fully coupled Eikonal-Reaction-Mechanics (ERM) model. In Sec. 3, we present the numerical approximation of the proposed ERM model. In Sec. 4, we present the numerical results and some comparisons with the EM model using the monodomain model.

2. Mathematical Model

From a phenomenological perspective, EP affects the active force generation through the calcium concentration in cardiomyocytes, within the so called *excitation-contraction coupling* process.[6] In a multiscale context, the active tension generated in the cells determines the contraction of the tissue. The mechanical model induces some feedback both on active force generation and on EP, the most relevant one implying that action potential propagates in a moving domain. Since in our EM model EP is solved by means of a steady Eikonal problem, we cannot take into account such a feedback, which is not a significant limitation in those contexts where no cardiac arrhythmias are present.[23,24,28]

Based on the latter consideration and starting from the strategy presented in Ref. 61, we propose in what follows our model for EM coupled with blood circula-

tion, see Figure 1.

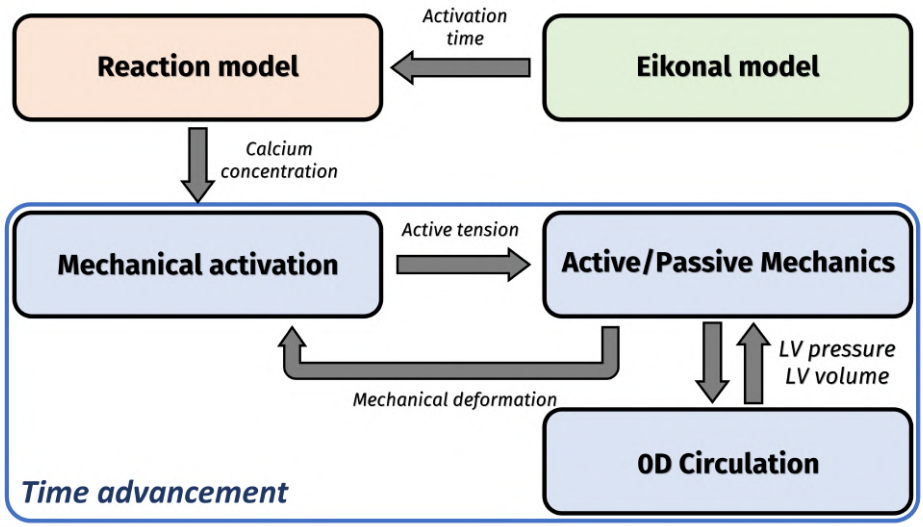

Fig. 1. General structure of the ERM model proposed in this work. In the green box we report the first numerical step of our strategy consisting in the solution of the Eikonal model. The second step, in the orange box, consists in the offline solution of the monodomain-like reaction model. The final step, in the blue box, consists in the time advancement which involves the active force generation, the active and passive mechanics and the coupling with the systemic circulation.

Let $\Omega \subset \mathbb{R}^3$ be a left ventricular domain with the boundary $\partial\Omega$ composed by the endocardium Γ^{endo}, the epicardium Γ^{epi}, and the base Γ^{base}, see Figure 2.

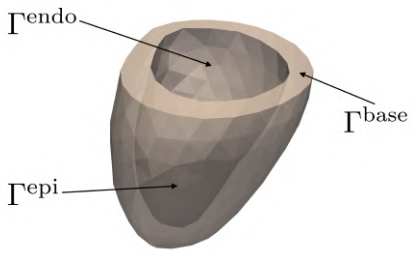

Fig. 2. Computational domain Ω: LV 3D geometry.

2.1. *Eikonal model*

We model the electrical activity of the LV with the following *Eikonal-diffusion* equation,[20,46] (Figure 1 green box):

$$\begin{cases} c_0\sqrt{\nabla\psi\cdot\frac{1}{\chi C_m}\boldsymbol{D}\nabla\psi}-\varepsilon\nabla\cdot\left(\frac{1}{\chi C_m}\boldsymbol{D}\nabla\psi\right)=1 & \text{in } \Omega,\\ \left(\frac{1}{\chi C_m}\boldsymbol{D}\nabla\psi\right)\cdot\boldsymbol{n}=0 & \text{on } \partial\Omega\setminus S_a,\\ \psi=\psi_a & \text{on } S_a, \end{cases} \tag{2.1}$$

where $\psi:\Omega\to\mathbb{R}$ is the unknown activation time, S_a is the portion of the physical boundary where the activation time ψ_a is prescribed, surrogating the effect of the Purkinje network[10,17,41,66] and $\boldsymbol{n}$ the outward directed unit vector normal to the boundary $\partial\Omega$ of the domain Ω. In system (2.1), the conductivity tensor $\boldsymbol{D}$ is defined as

$$\boldsymbol{D}=\sigma_f\boldsymbol{f}_0\otimes\boldsymbol{f}_0+\sigma_s\boldsymbol{s}_0\otimes\boldsymbol{s}_0+\sigma_n\boldsymbol{n}_0\otimes\boldsymbol{n}_0, \tag{2.2}$$

where σ_f, σ_s and σ_n are the conductivities along the fibers $\boldsymbol{f}_0$, the sheets $\boldsymbol{s}_0$, and the normal $\boldsymbol{n}_0$ directions, respectively. This local orthonormal coordinate system for the left ventricle can be generated using rule-based algorithms.[4,43] The constants χ and C_m represent the surface to volume ratio and the trans-membrane capacitance, whereas c_0 is associated with the velocity of the depolarization wave along the fiber direction for a planar wavefront and ε is a dimensionless parameter, being both uniform in the domain Ω.

Problem (2.1) will be compactly written as

$$\psi=\mathcal{E}(\psi_a).$$

2.2. *Reaction model*

In order to couple the Eikonal system (2.1) with an active force generation model, we need to compute the intracellular calcium ions concentration $[\mathrm{Ca}^{2+}]_i$ (see Figure 1 orange box) for every $(\boldsymbol{x},t)$ in $\Omega\times(0,T)$, where T is the final time. With this goal, we start by considering the monodomain model:[22]

$$\begin{cases} J\chi\left[C_m\dfrac{\partial u}{\partial t}+I_{\text{ion}}(u,\boldsymbol{w},\boldsymbol{z})\right]-\nabla\cdot\left(J\mathbf{F}^{-1}\mathbf{D}\mathbf{F}^{-T}\nabla u\right)=J\,I_{\text{app}}(\boldsymbol{x},t) & \text{in } \Omega\times(0,T),\\ \dfrac{d\boldsymbol{w}}{dt}=\boldsymbol{H}(u,\boldsymbol{w}) & \text{in } \Omega\times(0,T),\\ \dfrac{d\boldsymbol{z}}{dt}=\boldsymbol{G}(u,\boldsymbol{w},\boldsymbol{z}) & \text{in } \Omega\times(0,T),\\ \left(J\mathbf{F}^{-1}\mathbf{D}\mathbf{F}^{-T}\nabla u\right)\cdot\mathbf{N}=0 & \text{on } \partial\Omega\times(0,T), \end{cases} \tag{2.3}$$

where $u:\Omega\times(0,T)\to\mathbb{R}$ is the unknown transmembrane potential, $I_{\text{ion}}(u,\boldsymbol{w},\boldsymbol{z})$ is the ionic current modeled by means of a suitable ionic model,[22] $\boldsymbol{w}:\Omega\times(0,T)\to\mathbb{R}^r$ are the gating variables, $\boldsymbol{z}:\Omega\times(0,T)\to\mathbb{R}^s$ are the ionic concentrations, $\boldsymbol{H}\in\mathbb{R}^r$ and $\boldsymbol{G}\in\mathbb{R}^s$ are functions which depend on the specific ionic model. The anisotropic

diffusion tensor $\mathbf{D}$ encodes the electrical conductivity in the different directions, while $\mathbf{F}$ denotes the deformation gradient of the tissue, to be defined in Section 2.4 and J its Jacobian.

We then consider the following simplified version of the monodomain model (2.3), obtained by neglecting the diffusion term:[37]

$$\begin{cases} \chi\left[C_m\dfrac{\partial u}{\partial t} + I_{\text{ion}}(u,\boldsymbol{w},\boldsymbol{z})\right] = I_{\text{app}}(t-\psi(\boldsymbol{x})) & \text{in } \Omega\times(0,T_{\text{HB}}),\\ \dfrac{d\boldsymbol{w}}{dt} = \boldsymbol{H}(u,\boldsymbol{w}) & \text{in } \Omega\times(0,T_{\text{HB}}),\\ \dfrac{d\boldsymbol{z}}{dt} = \boldsymbol{G}(u,\boldsymbol{w},\boldsymbol{z}) & \text{in } \Omega\times(0,T_{\text{HB}}), \end{cases} \tag{2.4}$$

with periodic conditions $u(\boldsymbol{x},T_{\text{HB}}) = u(\boldsymbol{x},0)$, $\boldsymbol{w}(\boldsymbol{x},T_{\text{HB}}) = \boldsymbol{w}(\boldsymbol{x},0)$ and $\boldsymbol{z}(\boldsymbol{x},T_{\text{HB}}) = \boldsymbol{z}(\boldsymbol{x},0)$ for any $\boldsymbol{x}\in\Omega$, with T_{HB} being the heartbeat period, where $\psi(\boldsymbol{x})$ is the solution of the Eikonal model (2.1) and

$$I_{\text{app}}(t) = \begin{cases} \overline{I}_{\text{app}} & \text{if } 0 \le \text{mod}(t,T_{\text{HB}}) < \delta_{\text{stim}},\\ 0 & \text{otherwise,} \end{cases} \tag{2.5}$$

for suitable prescribed constant values $\overline{I}_{\text{app}}$ and δ_{stim}. The function mod denotes the modulo operation (i.e. remainder after division) and encodes the periodicity of the applied current. Furthermore, the periodic conditions ensure that the solution corresponds to a limit cycle of the ionic model.[53] In this way, we are localizing an applied current for each point $\boldsymbol{x}$ in a temporal neighborhood of $\psi(\boldsymbol{x})$, i.e. the time of activation of $\boldsymbol{x}$. The introduction of this chain of internal currents surrogates the physical process described by the diffusion term (here neglected) in the standard monodomain problem.

The solution of (2.4) requires, in principle, the solution in the infinite points of the domain (after introducing the finite element space discretization, this will boil down solving it at the mesh nodes).[37] This makes the approach still quite heavy from the computational point of view. To lighten this, we propose an efficient way to solve it. We notice that in (2.4) the spatial points are decoupled from each other (no spatial correlation exists). Hence, we propose to solve the equation in a single point (that is, in a 0D manner):

$$\chi\left[C_m\frac{du^{0\text{D}}}{dt} + I_{\text{ion}}(u^{0\text{D}},\boldsymbol{w}^{0\text{D}},\boldsymbol{z}^{0\text{D}})\right] = I_{\text{app}}(t), \qquad \text{in } (0,T), \tag{2.6a}$$

$$\frac{d\boldsymbol{w}^{0\text{D}}}{dt} = \boldsymbol{H}(u^{0\text{D}},\boldsymbol{w}^{0\text{D}}), \qquad \text{in } (0,T), \tag{2.6b}$$

$$\frac{d\boldsymbol{z}^{0\text{D}}}{dt} = \boldsymbol{G}(u^{0\text{D}},\boldsymbol{w}^{0\text{D}},\boldsymbol{z}^{0\text{D}}) \qquad \text{in } (0,T), \tag{2.6c}$$

with periodic conditions $u^{0\text{D}}(T_{\text{HB}}) = u^{0\text{D}}(0)$, $\boldsymbol{w}^{0\text{D}}(T_{\text{HB}}) = \boldsymbol{w}^{0\text{D}}(0)$ and $\boldsymbol{z}^{0\text{D}}(T_{\text{HB}}) = \boldsymbol{z}^{0\text{D}}(0)$. Then, we recover the solution in each point $\boldsymbol{x}\in\Omega$ by shifting in time the functions $u^{0\text{D}}$, $\boldsymbol{w}^{0\text{D}}$ and $\boldsymbol{z}^{0\text{D}}$ according to the time of activation of each point of the

domain:

$$\begin{aligned} u(\boldsymbol{x},t) &= u^{0\mathrm{D}}(t-\psi(\boldsymbol{x})),\\ \boldsymbol{w}(\boldsymbol{x},t) &= \boldsymbol{w}^{0\mathrm{D}}(t-\psi(\boldsymbol{x})),\\ \boldsymbol{z}(\boldsymbol{x},t) &= \boldsymbol{z}^{0\mathrm{D}}(t-\psi(\boldsymbol{x})), \end{aligned} \tag{2.7}$$

where the 0D solution has been periodically extended outside the interval $[0, T_{\mathrm{HB}}]$. We remark that since problem (2.6) is independent of the point $\boldsymbol{x}$, is can be pre-computed off-line, with a significant saving in the computational costs.

Once we have computed $(u, \boldsymbol{w}, \boldsymbol{z})$, we can identify a single concentration variable of $\boldsymbol{z}$ (or combination of them) as the intracellular calcium ions concentration:

$$[\mathrm{Ca}^{2+}]_i(\boldsymbol{x},t) = [\mathrm{Ca}^{2+}]_i^{0\mathrm{D}}(t-\psi(\boldsymbol{x})). \tag{2.8}$$

Problem given by (2.7)-(2.6)-(2.8) will be compactly written as

$$[\mathrm{Ca}^{2+}]_i = \mathcal{R}(\psi).$$

2.3. *Mechanical activation model*

We model the force generation in the cardiac muscle tissue with the physics-based active force model RDQ20-MF,[50] which takes advantage of a biophysically detailed representation of the proteins in the sarcomeres (Figure 1 blue box). This reads as follows:

$$\frac{d\boldsymbol{s}}{dt} = \boldsymbol{K}\left(\boldsymbol{s}, [\mathrm{Ca}^{2+}]_i, SL, \frac{dSL}{dt}\right) \qquad \text{in } \Omega\times(0,T), \tag{2.9}$$

with $\boldsymbol{s}(0) = \boldsymbol{s}_0$ in Ω at $t = 0$. The vectorial functions $\boldsymbol{s} : \Omega\times(0,T) \to \mathbb{R}^{20}$ represent the 20 state variables of the RDQ20-MF model. The latter describe the chemical and mechanical states of the regulatory (troponin and tropomyosin) and contractile (actin and myosin) proteins concurring at the sarcomere function. The ODE system (2.9) takes as input the calcium variable $[\mathrm{Ca}^{2+}]_i$ defined in (2.8) and the sarcomere length SL. The latter is determined by the local tissue stretch in the fiber direction, as we will explain later in Sect. 2.4. We here emphasize the dependence of the activation model on the variable $\boldsymbol{d}$, which describes the tissue displacement and which is the solution of the mechanical model described in Sect. 2.4. The generated active tension (denoted by T_a), which is the input of the mechanical model in Sect. (2.4), can be computed from the state $\boldsymbol{s}$ and the sarcomere length SL as follows

$$T_a = G(\boldsymbol{s}, SL), \tag{2.10}$$

where G is a suitable nonlinear function.[50]

Problem given by (2.9)–(2.10) will be compactly written as

$$T_a = \mathcal{F}([\mathrm{Ca}^{2+}]_i, \boldsymbol{d}).$$

2.4. *Active and passive mechanics models*

We model the dynamics of the displacement $\boldsymbol{d} : \Omega \times (0,T) \to \mathbb{R}^3$ of the tissue by the momentum conservation equation:[40]

$$\begin{cases} \rho \dfrac{\partial^2 \boldsymbol{d}}{\partial t^2} - \nabla \cdot \mathbf{P}(\boldsymbol{d}, T_a) = \mathbf{0} & \text{in } \Omega \times (0,T), \quad (2.11a) \\ \mathbf{P}(\boldsymbol{d}, T_a)\boldsymbol{n} + \mathbf{K}^{\text{epi}}\boldsymbol{d} + \mathbf{C}^{\text{epi}} \dfrac{\partial \boldsymbol{d}}{\partial t} = \mathbf{0} & \text{on } \Gamma^{\text{epi}} \times (0,T), \quad (2.11b) \\ \mathbf{P}(\boldsymbol{d}, T_a)\boldsymbol{n} = -p_{\text{LV}}(t) J \mathbf{F}^{-T} \boldsymbol{n} & \text{on } \Gamma^{\text{endo}} \times (0,T), \quad (2.11c) \\ \mathbf{P}(\boldsymbol{d}, T_a)\boldsymbol{n} = p_{\text{LV}}(t)\, |J\mathbf{F}^{-T}\boldsymbol{n}|\, \boldsymbol{v}^{\text{base}}(t) & \text{on } \Gamma^{\text{base}} \times (0,T), \quad (2.11d) \end{cases}$$

with $\boldsymbol{d} = \boldsymbol{d}_0$ and $\dfrac{\partial \boldsymbol{d}}{\partial t} = \dot{\boldsymbol{d}}_0$ in Ω at $t = 0$. The Piola-Kirchhoff stress tensor $\mathbf{P} = \mathbf{P}(\boldsymbol{d}, T_a)$ includes both the passive and active mechanics in the following form:

$$\mathbf{P}(\boldsymbol{d}, T_a) = \frac{\partial \mathcal{W}(\mathbf{F})}{\partial \mathbf{F}} + T_a \frac{\mathbf{F}\boldsymbol{f}_0 \otimes \boldsymbol{f}_0}{\sqrt{\mathcal{I}_{4f}}}, \quad (2.12)$$

with $\mathbf{F} = \mathbf{I} + \nabla \mathbf{d}$ the deformation tensor. The first term of (2.12) represents the passive part, the second one represents an *active stress* formulation for the active part,[36] and the term T_a is the active tension provided by the mechanical activation, see Sect. 2.3. The fourth invariant $\mathcal{I}_{4f} = \mathbf{F}\boldsymbol{f}_0 \cdot \mathbf{F}\boldsymbol{f}_0$ is a measure of the tissue elongation along the fibers direction. The strain energy density function W is modeled by the Guccione constitutive law $\mathcal{W}(\mathbf{F}) = \frac{C}{2}(e^Q - 1)$, with $C = \mathbf{F}^T\mathbf{F}$ the right Cauchy-Green deformation tensor and Q as in Ref. 26.

Boundary condition (2.11b) models the interaction of the LV with the pericardium,[42] defining the tensors:

$$\mathbf{K}^{\text{epi}} = K_{\perp}^{\text{epi}}(\boldsymbol{n} \otimes \boldsymbol{n}) + K_{\parallel}^{\text{epi}}(\boldsymbol{I} - \boldsymbol{n} \otimes \boldsymbol{n}), \quad (2.13a)$$

$$\mathbf{C}^{\text{epi}} = C_{\perp}^{\text{epi}}(\boldsymbol{n} \otimes \boldsymbol{n}) + C_{\parallel}^{\text{epi}}(\boldsymbol{I} - \boldsymbol{n} \otimes \boldsymbol{n}). \quad (2.13b)$$

$K_{\perp}^{\text{epi}}$, $K_{\parallel}^{\text{epi}}$, $C_{\perp}^{\text{epi}}$, $C_{\parallel}^{\text{epi}}$ are the positive constant local values of stiffness and viscosity of the epicardium in the normal and tangent directions.

Eqs. (2.11c) and (2.11d) represent the boundary conditions at the endocardium and the base, respectively, where $p_{LV}(t)$ is the blood pressure provided by the 0D model (Sect. 2.5), whereas $\boldsymbol{v}^{\text{base}}(t) = \int_{\Gamma^{\text{endo}}} J\mathbf{F}^{-T}\boldsymbol{n} d\Gamma / \int_{\Gamma^{\text{base}}} \|J\mathbf{F}^{-T}\boldsymbol{n}\| d\Gamma$ allows for the definition an energy-consistent boundary condition.[51] The local sarcomere length SL, which is an input for the active force generation, is determined starting from the sarcomere length at rest SL_0 as $SL = SL_0\sqrt{\mathcal{I}_{4f}}$.

Problem given by (2.11) will be compactly written as

$$\boldsymbol{d} = \mathcal{M}(T_a, p_{LV}, \boldsymbol{d}),$$

where the implicit dependence on $\boldsymbol{d}$ refers to the nonlinearity induced by the constitutive law in (2.12).

Remark 2.1. We highlight that problem (2.11) should be written in the *stress-free configuration* domain Ω, i.e. the domain without any blood pressure action. This is

crucial for the evaluation of the Piola-Kirchhoff tensor (2.12) at the right working points in the stress-strain non-linear curve. Thus, the LV geometry Ω_{clin} usually reconstructed from clinical images should be virtually deflated by the diastolic blood pressure in order to obtain a stress-free configuration Ω.[15,25,54]

2.5. *Circulation model*

We finally model the hemodynamics of the circulatory system dividing the heartbeat into four phases, starting the cardiac cycle at systole, following the model proposed in.[51] In particular, this gives the pressure $p_{LV}^{0\mathrm{D}} = p_{LV}$ which provides the boundary datum for the mechanics, see (2.11):

- Phase 1 - isovolumetric contraction: we solve problem (2.11) under the constraint $V_{LV}^{3D} = EDV$, where EDV represents the imposed end-diastolic volume, and where $p_{LV}^{0\mathrm{D}}$ is determined as the Lagrange multiplier enforcing the constraint;
- Phase 2 - ejection: the aortic valve opens when the pressure value has reached the fixed value $\overline{p}_{\mathrm{AVO}}^{0\mathrm{D}}$ at time instant t_{AVO}. It closes at the time instant t_{AVC}, when the flow rate becomes retrograde. From t_{AVO} to t_{AVC} (both unknown and determined by the coupling), we model the pressure evolution with the two-element windkessel model:[69]

$$C\frac{dp_{LV}^{0\mathrm{D}}}{dt} + \frac{1}{R}p_{LV}^{0\mathrm{D}} = \frac{dV_{LV}^{3D}}{dt} \qquad t \in (t_{\mathrm{AVO}}, t_{\mathrm{AVC}}). \tag{2.14}$$

  where R represents the total peripheral resistance and C the total arterial compliance. At time instant t_{AVC}, the first time instant in which $\frac{dV_{LV}^{3D}}{dt}$ changes its sign, we define $p_{LV}^{0\mathrm{D}}(t_{\mathrm{AVC}}) = \overline{p}_{\mathrm{AVC}}^{0\mathrm{D}}$;
- Phase 3 - isovolumetric relaxation: we solve problem (2.11) under the constraint $V_{LV}^{3D} = ESV$, where ESV represents the end-systolic volume reached at the end of phase 2, until $p_{LV}^{0\mathrm{D}} = \overline{p}_{\mathrm{MVO}}^{0\mathrm{D}}$ when the mitral valve opens;
- Phase 4 - filling: we linearly increase the pressure $p_{LV}^{0\mathrm{D}}$ until the prescribed value $\overline{p}_{\mathrm{ED}}^{0\mathrm{D}}$ (representing the end diastolic pressure) is reached at the end of the cardiac cycle.

The volume $V_{LV}^{3D}(t) = V_{LV}^{3D}(\boldsymbol{d}(t))$ in Eq. (2.14) represents the volume of the LV in the 3D model computed as:

$$V_{LV}^{3D}(t) = \int_{\Gamma^{\mathrm{endo}}} J(t)((\boldsymbol{h}\otimes\boldsymbol{h})(\boldsymbol{x}+\boldsymbol{d}(t)-\boldsymbol{b}))\cdot\mathbf{F}^{-T}(t)\mathbf{N}d\Gamma, \tag{2.15}$$

where $\boldsymbol{d}$ is the myocardial displacement, $\boldsymbol{h}$ a vector lying on the LV base and $\boldsymbol{b}$ the coordinate of an arbitrary point inside the LV.[54,55]

Problem (2.14) represents the flow rate continuity. The pressure continuity is given by conditions (2.11c)-(2.11d) in the mechanical problem.

Problem given by one of the phases described above (depending on the time instant in the cardiac cycle) together with Eq. (2.15) will be compactly written as

$$p_{LV} = \mathcal{C}(\boldsymbol{d}).$$

2.6. *Review of the global problem*

According to the notations introduced above, we summarize in a compact way the full ERM model given by (2.1)-(2.6)-(2.8)-(2.9)-(2.11)-(2.14)-(2.15) proposed in the previous sections as follows:

$$\begin{cases} \text{Steady Eikonal} & \psi = \mathcal{E}(\psi_a), \quad (2.16a) \\ \text{Dynamic Electrophysiology} & [\mathrm{Ca}^{2+}]_i = \mathcal{R}(\psi), \quad (2.16b) \\ \text{Active tension} & T_a = \mathcal{F}([\mathrm{Ca}^{2+}]_i, \boldsymbol{d}), \quad (2.16c) \\ \text{Mechanics} & \boldsymbol{d} = \mathcal{M}(T_a, p_{LV}, \boldsymbol{d}), \quad (2.16d) \\ \text{0D circulation model} & p_{LV} = \mathcal{C}(\boldsymbol{d}). \quad (2.16e) \end{cases}$$

By substituting the other relations into (2.16d), we obtain the following fixed-point problem for the myocardial displacement $\boldsymbol{d}$, which highlights the dependence on the sole input ψ_a:

$$\boldsymbol{d} = \mathcal{M}(\mathcal{F}(\mathcal{R}(\mathcal{E}(\psi_a)), \boldsymbol{d}), \mathcal{C}(\boldsymbol{d}), \boldsymbol{d}).$$

The overall coupled problem is graphically reviewed in Figure 3.

Here, we can appreciate that the EP problem is independent from the other subproblems, since we have no feedback from the mechanics; in particular we are neglecting that the EP problem should be solved in a moving configuration. The accuracy of this modeling assumption will be investigated in Section 4 by means of numerical tests.

3. Numerical approximation

The ERM model (2.16) has been numerically approximated by a segregated method, based on a loosely-coupled strategy for both mechanics/activation and mechanics/0D model couplings. This choice was made in order to use pre-existing available codes and to address different spatial and temporal scales associated to the each described process. Notice that the EP subproblem is already segregated at the level of the continuous problem.

Regarding the time discretization of the ERM model (2.16), we discretized all the evolutionary problems with the Backward Differentiation Formula (BDF) scheme of order 1. With this aim, we considered a time step Δt for problems (2.16c)-(2.16d)-(2.16e). At each time step, problem (2.16c), that requires a finer time step for numerical stability purposes, is advanced resorting to an inner iteration loop, according to the scheme proposed in Ref. 50.

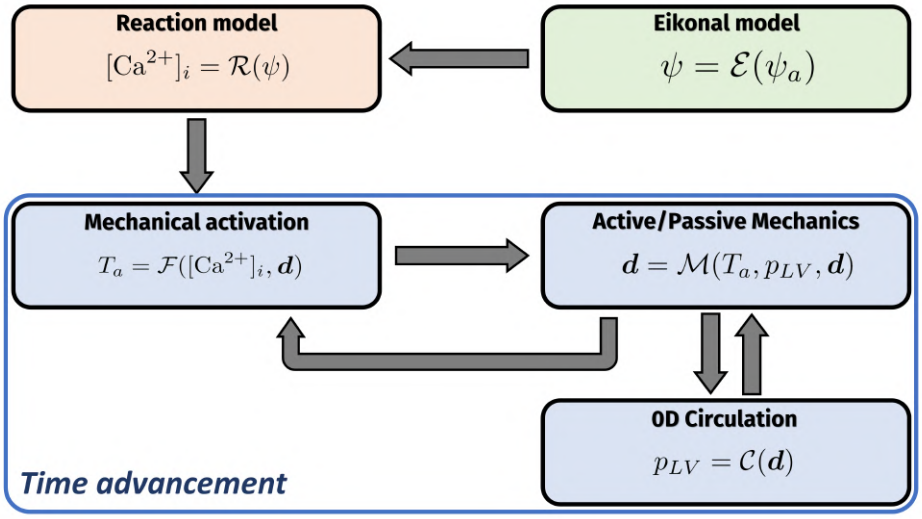

Fig. 3. General structure of the ERM model proposed in this work, highlighting the compact version of the involved mathematical systems.

Given a function of time $\alpha(t)$, we will denote by $\alpha^n \simeq \alpha(t^n)$ its approximation at $t^n = n\Delta t$.

Regarding the solution of the steady Eikonal problem (2.1), we obtained it as the steady-state solution of the following parabolic problem:

$$\frac{\partial \psi}{\partial \tau} + c_0 \sqrt{\nabla \psi \frac{1}{\chi C_m} \boldsymbol{D} \nabla \psi} - \varepsilon \nabla \cdot \left(\frac{1}{\chi C_m} \boldsymbol{D} \nabla \psi \right) = 1,$$

with the same boundary and initial conditions as in (2.1) and where τ is the pseudo-time. The time discretization of such problem has been performed using a fully implicit BDF scheme of order 1 used in combination with the Newton algorithm.

The time discretization of (2.16b) was based on the BDF scheme of order 1 for problem (2.6a) and the first order implicit-explicit (IMEX) scheme with an explicit treatment of the ionic concentrations and an implicit treatment of the gating variables for the ionic current problems (2.6b)-(2.6c).[2] Notice that to obtain the calcium concentration for any time and at any spatial point, it is enough to solve only the ODE problem (2.6), whose solution is independent of the computational domain.

The space discretization of each subproblem has been performed through Finite Element Method (FEM)[48] of order 1 on hexahedral meshes (Q1). The resulting linear systems arising at each time step have been solved by the GMRES method preconditioned with the AMG preconditioner.[8,56] We considered a coarser representation of the computational domain for the active force generation and the mechanics models (2.16c)-(2.16d), whereas a finer one for the Eikonal diffusion model

(2.16a) according to the need of capturing the propagating front. Specifically, we considered two nested hexahedral meshes, generating the finer one by a uniform refinement of the coarser one, recursively splitting each element into eight sub-elements until the reaching of the desired refinement (about 0.8 mm for the mesh length).[9]

Summarizing, setting $N = \frac{T}{\Delta t}$ the total number of time steps, we propose Algorithm 1 (see also Figure 4):

Algorithm 1: Solution of the ERM model

Given ψ_a solve the Eikonal problem $\psi_h = \mathcal{E}_h(\psi_a)$;
Solve the ODE model (2.5)-(2.6) and build the calcium concentration $[\mathrm{Ca}^{2+}]_{i,h} = \mathcal{R}_h(\psi_h)$;
for $0 \leq n < N$ **do**
  Interpolate in time $[\mathrm{Ca}^{2+}]_{i,h}$ to obtain $[\mathrm{Ca}^{2+}]^n_{i,h}$;
  Compute $T^{n+1}_{a,h} = \mathcal{F}^{n+1}_h([\mathrm{Ca}^{2+}]^n_{i,h}, \boldsymbol{d}^n_h)$;
  if isovolumetric contraction **then**
    Compute $(p^{n+1}_{LV}, \boldsymbol{d}^{n+1}_h)$ solving $\begin{cases} \boldsymbol{d}^{n+1}_h & = \mathcal{M}^{n+1}_h(T^{n+1}_{a,h}, p^{n+1}_{LV}, \boldsymbol{d}^{n+1}_h), \\ V^{n+1}_{LV} & = V^n_{LV}, \end{cases}$
    until $p^{n+1}_{LV} = \overline{p}_{\mathrm{AVO}}$;
  else if ejection **then**
    Compute p^{n+1}_{LV} solving (2.14) until $\frac{dV}{dt}(t^{n+1}) \simeq \frac{V^{n+1}-V^n}{dt}$ changes its sign;
    Compute $\boldsymbol{d}^{n+1}_h = \mathcal{M}^{n+1}_h(T^{n+1}_{a,h}, p^{n+1}_{LV}, \boldsymbol{d}^{n+1}_h)$;
  else if isovolumetric relaxation **then**
    Compute $(p^{n+1}_{LV}, \boldsymbol{d}^{n+1}_h)$ solving $\begin{cases} \boldsymbol{d}^{n+1}_h & = \mathcal{M}^{n+1}_h(T^{n+1}_{a,h}, p^{n+1}_{LV}, \boldsymbol{d}^{n+1}_h), \\ V^{n+1}_{LV} & = V^n_{LV}, \end{cases}$
    until $p^{n+1}_{LV} = \overline{p}_{\mathrm{MVO}}$;
  else if filling **then**
    Linearly increase p^{n+1}_{LV} until $p_{LV} = \overline{p}_{\mathrm{ED}}$;
    Compute $\boldsymbol{d}^{n+1}_h = \mathcal{M}^{n+1}_h(T^{n+1}_{a,h}, p^{n+1}_{LV}, \boldsymbol{d}^{n+1}_h)$.
end

We remark that in the isovolumetric contraction and isovolumetric relaxation phases, problem (2.11) is solved under the constraint $V^{n+1}_{LV} = V^n_{LV}$, leading to a saddle-point problem. We solved it by means of a Schur complement reduction.[5,51] In Algorithm 1, the operators $\mathcal{E}_h$ and $\mathcal{R}_h$ represent the discretized counterparts of the corresponding continuous operators, introduced above. Similarly, $\mathcal{F}^{n+1}_h$, $\mathcal{C}^{n+1}_h$ and $\mathcal{M}^{n+1}_h$ represent the operators associated with the time advancement numerical scheme from time t_n to time t_{n+1}, after space discretization, for the force generation, circulation and mechanical models, respectively. Notice that the dependence on the variables at previous iterations is understood.

The non-linear problem

$$\boldsymbol{d}_h^{n+1} = \mathcal{M}_h^{n+1}(T_{a,h}^{n+1}, p_{LV}^{n+1}, \boldsymbol{d}_h^{n+1})$$

is solved by using the Newton algorithm.[47]

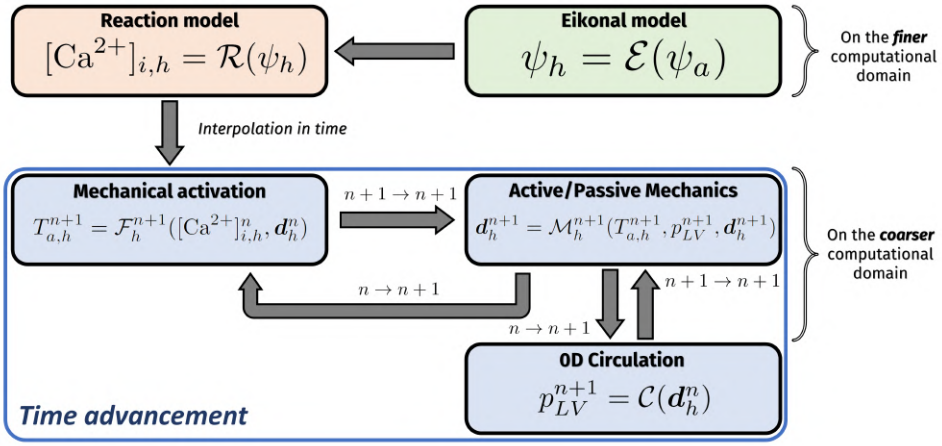

Fig. 4. General structure of the algorithm for solving the ERM model proposed in this work.

All the numerical methods involved in the presented ERM model have been implemented within `life`$^{\mathrm{x}}$ (`https://lifex.gitlab.io`), a in-house developed high-performance `C++` library mainly focused on cardiac applications, based on the `deal.II` Finite Element core.[1]

4. Numerical results

We now present the numerical results obtained with the ERM model proposed in the previous sections and with the EM-Monodomain model obtained by using the (discretized) monodomain problem (2.3) instead of the Eikonal-reaction one. The geometry for the computational domain has been segmented from the Zygote Solid 3D heart.[30] All the meshes (the finer and the coarser ones) were generated using the `vmtk` tool (`www.vmtk.org`) by means of a set of new meshing generation tools.[18] We used the following space and time discretization parameters: $h = 0.85\,\mathrm{mm}$ for the finer mesh, $h = 3.4\,\mathrm{mm}$ for the coarser mesh and $\Delta t = 10^{-4}s$ for the time step . All the numerical results have been obtained using the available HPC resource at MOX Laboratory, Politecnico di Milano. The simulations of the ERM model were ran on 20 Intel Xeon E5-2640 v4 CPUs, while the simulation of the EM-monodomain model were run on 56 Intel Xeon Gold 6238 CPUs.

To trigger the action potential propagation, we applied an electrical current at three points located at the endocardial septum of the LV, as depicted in Figure 5.

The stimulation configuration has been employed in order to mimic the functioning of the Purkinje network in the LV,[14,66,67] which is not included in the presented mathematical model. Specifically, we selected the radius of the stimuli equal to 0.6 mm and a delay between them in order to reproduce the conduction velocity of about $500\,\mathrm{cm\,s^{-1}}$ in the Purkinje network.[31,65] To fulfill the periodic boundary conditions of the Reaction problem (2.6), we performed 1000 cycles, with the 18-variables ten Tusscher-Panfilov ionic model,[63] in order to reach a limit cycle (i.e. a periodic solution). The last cardiac cycle has been then extracted as the reference one to compute the calcium ion concentration. We report all parameters related to the EP model in Tab. 1. We here denote by $\hat{\sigma}_\alpha = \sigma_\alpha/(C_m\chi)$, for $\alpha \in \{f, s, n\}$ the normalized conductivities and by $\overline{\mathcal{I}}_{\text{app}} = \overline{I}_{\text{app}}/(C_m\chi)$ the normalized applied current magnitude.

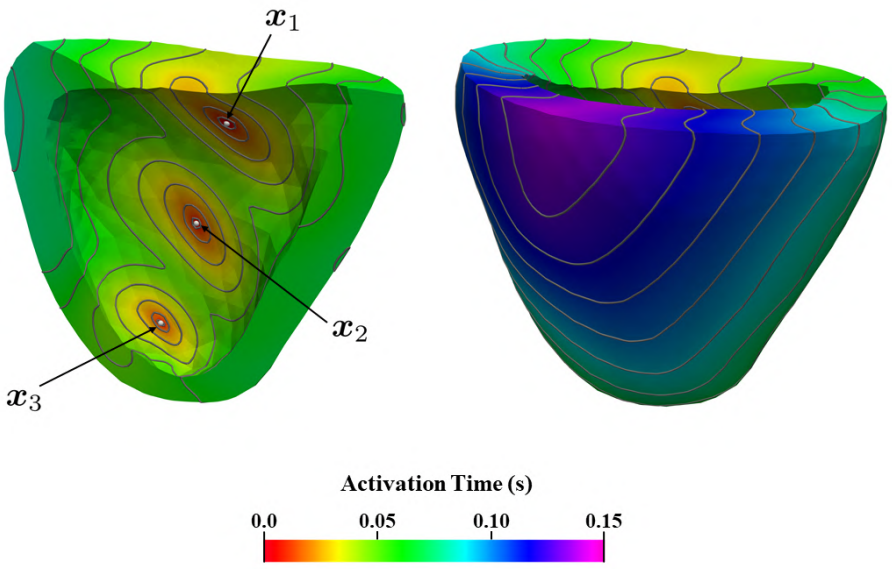

Fig. 5. Location of stimulation sites and activation map in the LV.

$\hat{\sigma}_f$ $(\mathrm{m^2\,s^{-1}})$	$\hat{\sigma}_s$ $(\mathrm{m^2\,s^{-1}})$	$\hat{\sigma}_n$ $(\mathrm{m^2\,s^{-1}})$	$\overline{\mathcal{I}_{\text{app}}}$ $(\mathrm{V\,s^{-1}})$	δ_{stim} (ms)
$1.529 \cdot 10^{-4}$	$0.699 \cdot 10^{-4}$	$0.225 \cdot 10^{-4}$	9.427	3
c_0 $(\mathrm{s^{-1/2}})$	ε	$\psi_a(\boldsymbol{x}_1)$ (ms)	$\psi_a(\boldsymbol{x}_2)$ (ms)	$\psi_a(\boldsymbol{x}_3)$ (ms)
62	7.5	0	5	10

Table 1. Electrophysiology model parameters.

Regarding the mechanical activation model (2.9), we employed the values reported in Ref. 50, with a crossbridge stiffness $a_{\text{XB}} = 1.6 \cdot 10^2$ MPa, which can be interpreted as the contractility of the cardiac muscle. We also set the following parameters: $\bar{k}_d = 0.4\,\mu\text{M}$, $\alpha_{k_d} = -0.2083\,\mu\text{M}\,\mu\text{m}^{-1}$, $\gamma = 30$, $k_{\text{off}} = 40\,\text{s}^{-1}$, $k_{\text{basic}} = 8\,\text{s}^{-1}$, $\mu^0_{f_\mathcal{P}} = 32.255\,\text{s}^{-1}$ and $\mu^1_{f_\mathcal{P}} = 0.768\,\text{s}^{-1}$. Finally, we reported in Tab. 2 all parameters related to the mechanical and circulation models.

$K_\perp^{\text{epi}}$ (Pa m^{-1})	$K_\parallel^{\text{epi}}$ (Pa m^{-1})	$C_\perp^{\text{epi}}$ (Pa s m^{-1})	$C_\parallel^{\text{epi}}$ (Pa s m^{-1})	SL_0 (µm)
$2 \cdot 10^5$	$2 \cdot 10^4$	$2 \cdot 10^4$	$2 \cdot 10^3$	2
R (Pa s m^{-3})	C (Pa^{-1} m^3)	$\overline{p}_{\text{ED}}$ (mmHg)	$\overline{p}_{\text{AVO}}$ (mmHg)	$\overline{p}_{\text{MVO}}$ (mmHg)
$5 \cdot 10^7$	$4.5 \cdot 10^{-9}$	10	83	5

Table 2. Mechanics and circulation models parameters.

Since the electrical propagation velocity is different along the fiber and crossfiber directions, the inclusion of the fiber orientation in the EM model plays a fundamental role in the propagation of the electrical signal. Standard MRI and CT imaging techniques do not provide information on the geometry distribution of the fibers, since thier spatial resolution is not fine enough. Hence, to estimate the fiber orientation we used the Bayer-Blake-Plank-Trayanova rule-based algorithm.[4] We used the following boundary values for the fibers and the sheets angles: $\alpha_{\text{epi}} = -60°$, $\alpha_{\text{endo}} = 60°$, $\beta_{\text{epi}} = 20°$ and $\beta_{\text{endo}} = -20°$.[43]

4.1. *Test I: Reference scenario*

We present the first numerical test. We calibrated the conductivities in the Eikonal model in order to reproduce physiological conduction velocity values (test I). Specifically, we obtained $0.63\,\text{m}\,\text{s}^{-1}$ along the longitudinal direction of the fibers, $0.42\,\text{m}\,\text{s}^{-1}$ along the transversal direction, and $0.2\,\text{m}\,\text{s}^{-1}$ along the normal direction.[59] In Figure 5 we show the corresponding activation map on the LV, with a focus on the stimulation areas on the septal epicardium. We performed 5 cardiac cycles ($T = 4\,\text{s}$) to study the convergence to a limit cycle of the ERM model. In Figure 6 we show the corresponding final PV loops. We notice that the limit cycle is attained at the second cardiac cycle. From now on, unless differently specified, all numerical results will correspond to the second cardiac cycle only.

In Figure 6, we also show the evolution in time of the LV pressure, fluid volume and solid volume. Specifically, analyzing the time evolution of the fluid volume and pressure, we notice the isovolumetric contraction phase, in which the volume of the chamber remains constant while the pressure increases due to the closure of the mitral valve. Then, the aortic valve opens and the volume of blood in the chamber rapidly decreases until the closure of the valve. The diastole starts and the volume reaches its minimum value and remains unchanged in the isovolumetric

relaxation phase in which the pressure decreases. Finally, the mitral valve opens and the chamber is filled with blood increasing its internal volume.

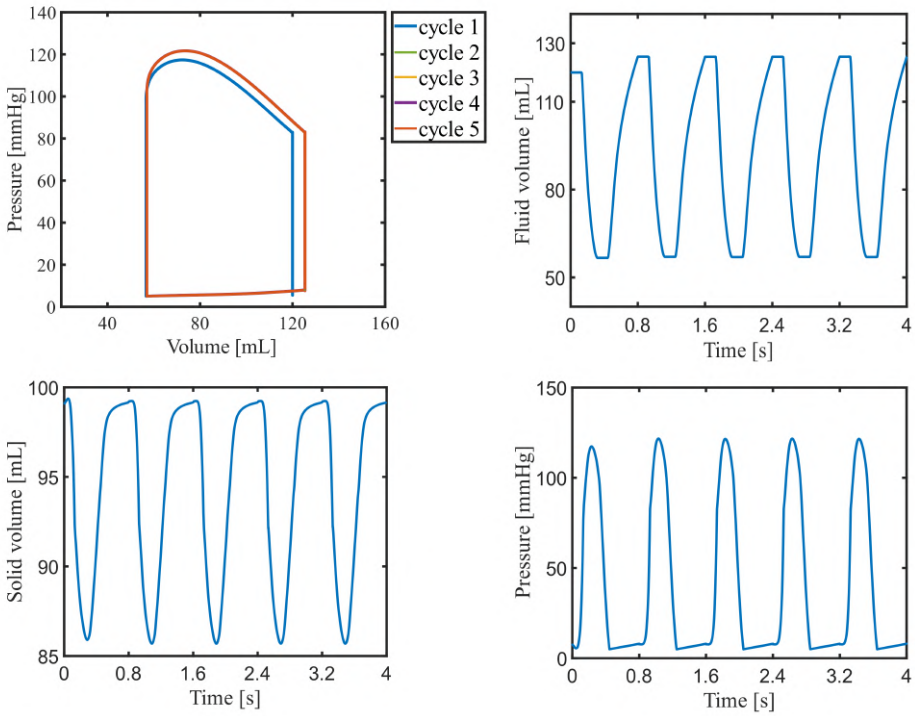

Fig. 6. Top left: left ventricle PV loops of 5 cardiac cycles. Top right: corresponding time evolution of fluid volume. Bottom left: time evolution of the solid volume. Bottom right: time evolution of the pressure in the LV. Test I.

To characterize the LV mechanical function and the associated PV loop, we introduce a set of biomarkers. Specifically, the maximum pressure in the ventricle $p_{\max}$; the end-diastolic volume (EDV), which represents the volume of blood in the ventricle at the end of the diastolic phase; the end-systolic volume (ESV), which represents the volume of blood at the end of the contraction; the stroke volume (SV), which is computed as $SV = EDV - ESV$ and which represents the volume of blood pumped from the ventricle in the cardiac cycle; the ejection fraction (EF), which is computed as $EF = SV/EDV \times 100$ and which represents the volumetric fraction of the blood ejected from the ventricle within a cardiac cycle. From Figure 6 we obtain the following values: $p_{\max} = 122\,\text{mmHg}$, $EDV = 127\,\text{mL}$, $ESV = 56\,\text{mL}$, $SV = 71\,\text{mL}$ and $EF = 56\%$. We want to underline that all these values are reached in the second heartbeat, starting from an initial imposed $EDV = 120\,\text{mL}$. All the obtained values lie within physiological ranges for the human LV.[34]

In addition, in Figure 7 we show the displacement on the LV computational domain at four different time instants during the heartbeat. We notice the filled ventricle at the initial time instant, in which the chamber has its maximum internal volume. Then, the ventricle contracts and reduces its volume, increasing its displacement. Finally the LV starts to relax decreasing its displacement.

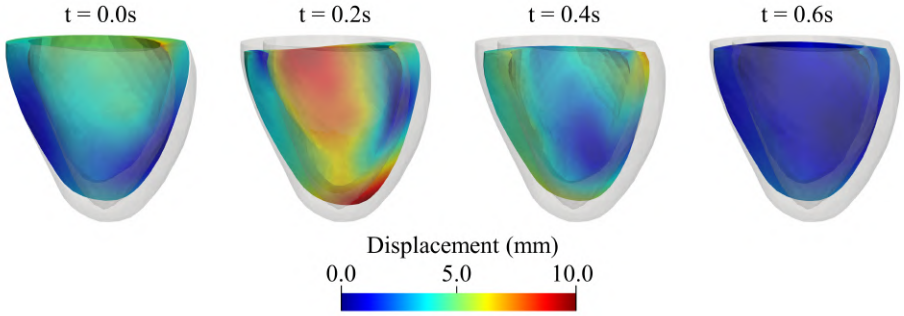

Fig. 7. Displacement on the LV domain at four time instants of the cardiac cycle: 0.0 s, 0.2 s, 0.4 s, 0.6 s. With a reduced opacity it is highlighted the LV volume at the initial time step. Test I.

We refer to the results obtained with test I, obtained using the values reported in Tabs. 1-2, as the reference scenario.

4.2. *Tests II, III, IV: Sensitivity analysis on mechanical parameters*

Then, we tested how our ERM model reacts to some different scenarios with respect to the reference one. We started varying the preload, by modifying the imposed $EDV = 120\,\text{mL}$ (test II). In Figure 8 (left) we show the obtained PV loop increasing the EDV by 20% at the top and decreasing the EDV by 20% at the bottom. In Tab. 3 we report all values obtained for the two scenarios. With respect to the reference scenario, we notice that the larger is EDV, the larger the maximum pressure $p_{\max}$ is. As a consequence, SV and EF follow the same trend.

Then, we varied the afterload by acting on the total peripheral resistance R in the windkessel model (test III). In Figure 8 (middle) are depicted the corresponding PV loops with an increased R by 20% (at the top) and a decreased R by 20% (at the bottom) with respect to the reference scenario. We can notice that increasing R directly increases $p_{\max}$ and ESV, and decreases SV and EF. Decreasing R yields to the opposite effect. This behavior is in agreement with the physiological meaning of the variation parameter. Increasing, or decreasing, the total peripheral resistance, means that an higher, or lower, pressure is needed in order to pump the blood out of the chamber. This may represent, for example, the effect of a vasoconstrictor or vasodilator drug, respectively.

We finally varied also the contractility value a_{XB} in the mechanical activation model (test IV). In Figure 8 (right) we show the PV loops with an increased a_{XB} by 20% (at the top) and a decreased a_{XB} by 20% (at the bottom) with respect to the reference scenario. We notice that increasing a_{XB} directly increases SV and EF and decreases ESV, while decreasing it provides the opposite effects. This is coherent with expectation, as well as increasing the contractility of the LV entails that the muscle is able to fill with more blood (increased SV) and to eject an higher amount of fluid (increased EF).

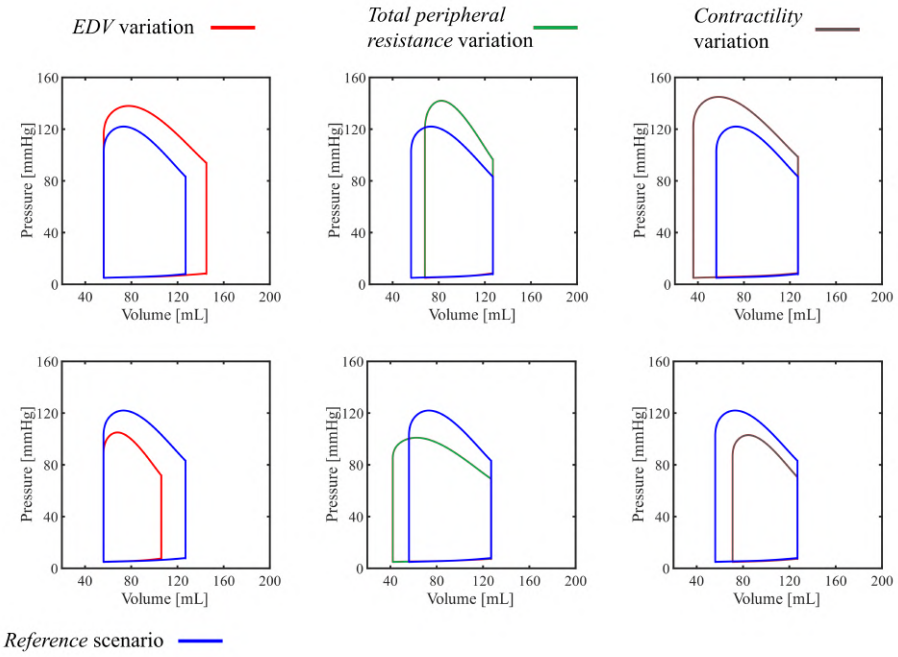

Fig. 8. PV loops in different scenarios: variations of EDV (left), variation of total peripheral resistance R (middle), variation of contractility a_{XB} (right). Top: increased parameters. Bottom: decreased parameters. All PV loops are compared with the reference scenario in blue. Test II (left), test III (middle), test IV (right).

4.3. *Test V: Abnormal variation of EDV*

We analyzed how the ERM model reacts to a huge variation in the EDV value, specifically increasing it by 50% (test V), see Figure 9. As we notice from Figure 9, on the left, the PV loop leads to non-physiological values of $SV = 129\,\mathrm{mL}$ and $EF = 70\%$, which are out of bounds with respect to physiological ranges.[34] We calibrated the other parameters (R and a_{XB}) in order to obtain physiological SV, still with an increased EDV. We set $R = 7 \cdot 10^7\,\mathrm{Pa\,s\,m^{-3}}$ and $a_{\mathrm{XB}} = 1.2 \cdot 10^2\,\mathrm{MPa}$.

	EDV [mL]	ESV [mL]	$p_{\max}$ [mmHg]	SV [mL]	EF [%]
Reference	127	56	122	71	56
EDV +20%	145	56	138	89	61
EDV −20%	106	56	105	50	47
R +20%	127	68	142	59	46
R −20%	127	42	101	85	67
a_{XB} +20%	127	36	145	91	72
a_{XB} −20%	127	71	103	56	44

Table 3. Mechanical bio-markers in the reference scenario (Test I) and in the considered variations parameters scenarios (Tests II, III, IV).

In Figure 9 right the final PV loop compared with the reference scenario one. We obtained a physiological $SV = 68\,\mathrm{mL}$. However, $EF = 32\,\%$ which is clearly out of range.[34]

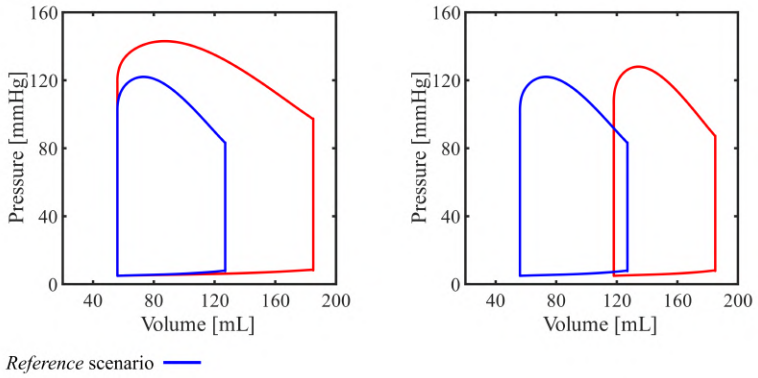

Fig. 9. PV loop obtained with an increased EDV (left) and after the calibration of the total peripheral resistance and contractility (right). Test V.

4.4. *Test VI: Simulation with grey zone and scar*

As an additional scenario, starting from the values in the reference scenario, we introduced in the LV geometry the presence of two sub-volumes with a reduced conductivity: the grey zone and the scar (test VI). With this goal, we intersected the LV with two spheres obtaining the configuration depicted in Figure 10 (top). Specifically, we multiplied the conductivity tensor $\boldsymbol{D}$ in (2.1) by a factor 0.5 for the grey zone and 0 for the scar in order to obtain areas with reduced conductivity and zero conductivity, respectively. In Figure 10 (bottom left) we show the activation map in the reduced conductivity scenario and the corresponding PV loop.

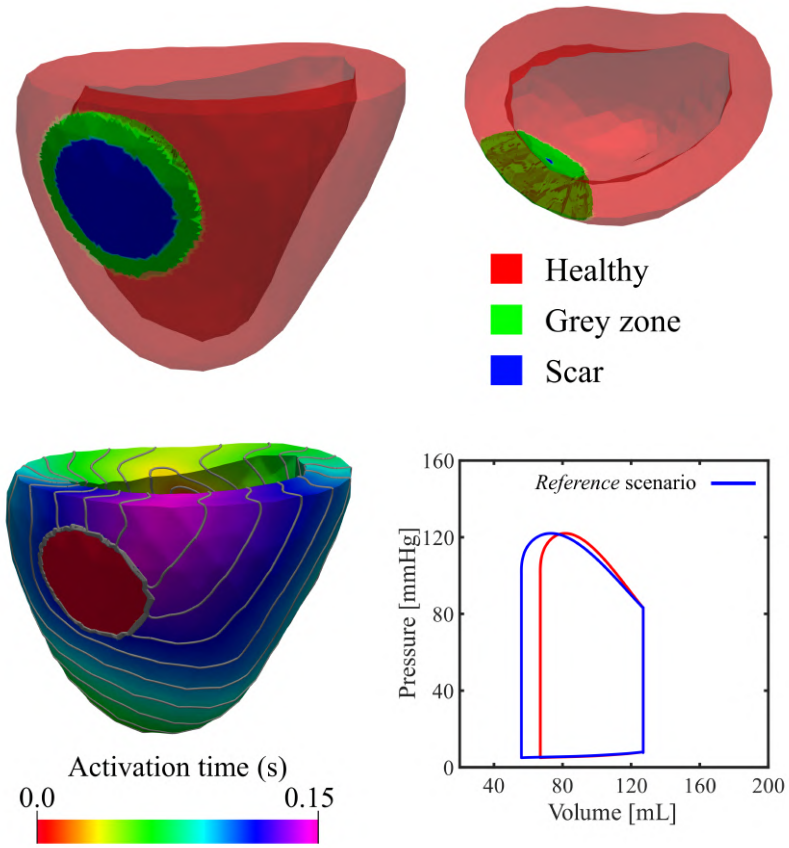

Fig. 10. Top: Geometric configuration in the reduced conductivity scenario. In red the healthy tissue, in green the grey zone with a reduced conducitivity, and in blue the scar with zero conduction. Bottom: Activation map in the reduced conductivity scenario (left) and PV loop, in red, with respect to the reference scenario one, in blue (right). Test VI.

We notice that the presence of the grey zone affected the activation time pattern with respect to the reference one, see Figure 5. Also by a mechanical point of view we obtained significant results. In Figure 10 (bottom right), the obtained PV loop (in red) is compared with the reference scenario one (in blue). We notice that the $p_{\max}$ remained almost unchanged, but the ESV increased. Specifically, we obtained $ESV = 67\,\text{mL}$, $SV = 60\,\text{mL}$ and $EF = 47\,\%$. As expected, the pumping ability of the LV was reduced: in the simulation a lower volume of blood was pumped out from the ventricle into the circulatory system.

4.5. *Tests VII-VIII: Comparison with EM-monodomain model*

As a final test, we compare the results of simulations obtained through the elec-

tromechanical model proposed in this paper with those obtained using the monodomain model rather than the Eikonal one, all other models and parameters being equal. First, we carry out this comparison in the reference setting, corresponding to physiological conditions (Test VII). More precisely, we perform two simulations. The first one is obtained through the models and methods presented in Sections 2 and 3 (ERM model). The second one, instead, is obtained by computing the intracellular calcium concentration through the solution of problem (2.3) rather than (2.4)-(2.5) (EM-monodomian model). For the numerical approximation of the latter, we refer the interested reader to.[54] For simplicity, we here consider only the first heartbeat. To perform the comparison, we calibrate the conductivities in the Eikonal and monodomain models, respectively, in such a way the latest activation time obtained with the two models is similar. As shown in Figure 11, the PV loops obtained in this setting with the two approaches are virtually overlapping. Table 4.5 shows that, for the mechanical bio-markers considered above, the ERM model provided very accurate results compared to the EM-monodomain model (relative difference of the order of 10^{-3}).

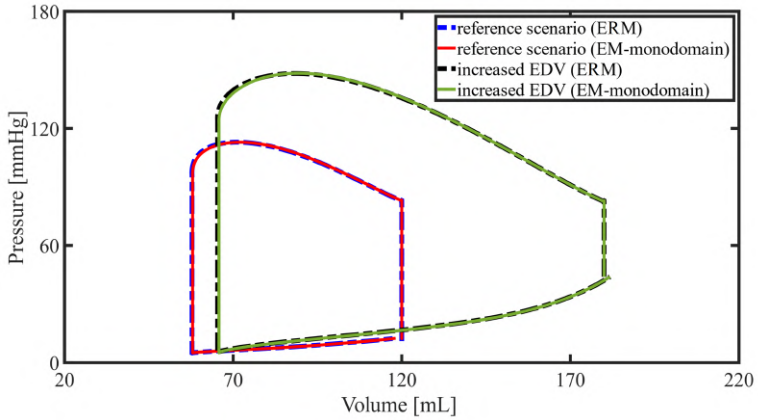

Fig. 11. Comparison of the results of two electromechanical simulations, obtained relying on the Eikonal model and monodomain model, respectively, to describe the wavefront propagation (tests VII and VIII).

To further test the ERM model as a surrogate for the EM-monodomain model, let us consider a pathological case, with an abnormally high EDV (Test VIII). This experiment is designed to accentuate the effects of mechano-electrical feedback, due to the large strains, which are ignored by construction in the Eikonal model, since (2.1) is solved in a fixed domain. Although this setting is particularly challenging for the Eikonal model, as shown in Figure 11, the latter model is able, when coupled with the mechanical model, to produce very accurate PV loops compared to those produced by the monodomain model. As shown in Table 4.5, the differences

between ERM and EM-monodomain results obtained in Test VIII are indeed only slightly larger than for test VII. We stress that, for fairness, we did not recalibrate the conductivities to perform this test, but used the same ones calibrated for the physiological case.

	EDV [mL]	ESV [mL]	$p_{\max}$ [mmHg]	SV [mL]	EF [%]
Test VII					
EM-monodomain	120.00	57.94	112.64	62.06	51.72
ERM	120.00	57.78	112.67	62.22	51.85
relative difference	0	$2.8 \cdot 10^{-3}$	$2.7 \cdot 10^{-4}$	$2.6 \cdot 10^{-3}$	$2.6 \cdot 10^{-3}$
Test VIII					
EM-monodomain	180.00	65.78	147.94	65.78	63.46
ERM	180.00	65.38	147.77	65.38	63.68
relative difference	0	$5.9 \cdot 10^{-3}$	$1.1 \cdot 10^{-3}$	$3.4 \cdot 10^{-3}$	$3.4 \cdot 10^{-3}$

Table 4. Mechanical bio-markers in tests VII and VIII: comparison between ERM and EM-monodomain models and relative differences.

4.6. *Computational times*

For the reference scenario and for all the tests that we analyzed with the ERM model, the total computational time for each cardiac cycle, on the available HPC resources cited above (20 cores), consists of: about 50 s for the Eikonal problem and about 9 h 30 min for the temporal loop part. The Reaction problem has been numerically solved once and for all in order to obtain the off-line calcium concentration for the ERM model, taking nearly 400 s on a single core. On the other hand, the simulations obtained with the EM-monodomain model took about 102 h hours with 56 cores. The EM-monodomain model therefore provides a very advantageous speedup, while remaining very accurate.

5. Conclusions

We presented a new electromechanical model for the cardiac function, based on a RE model, which enables an off-line solution of the Reaction problem. The efficient way to solve the Reaction problem leads to a reduction of the computational costs with respect to the standard electromechanical models. We coupled the EP part with a physics-based active force model, to better describe and characterize the coupling, and the mechanics with a windkessel model for blood circulation. We showed numerical results by focusing on the reproducibility of significant mechanical outputs. The ERM is able to provide a physiological response to variations in variables such as end-diastolic volume, total peripheral resistance, and contractility, with a low computational cost, thanks to solution of the Eikonal and the off-line

Reaction problems. Moreover, the model allows for the inclusion of domain regions with a reduced or zero conductivity. Finally, we showed that the ERM model is able to produce mechanical outputs that are accurate with respect to the outputs of the EM-monodomain model, in a reference setting and even in a setting where the role of mechano-electrical feedbacks - an aspect that the ERM model neglects by construction - is accentuated.

Acknowledgements

This project has received funding from the Italian research project MIUR PRIN17 2017AXL54F "Modeling the heart across the scales: from cardiac cells to the whole organ".

References

1. D. Arndt, W. Bangerth, T. Clevenger, D. Davydov, M. Fehling, D. Garcia-Sanchez, G. Harper, T. Heister, L. Heltai, M. Kronbichler, R. Kynch, M. Maier, J.-P. Pelteret, B. Turcksin and D. Wells, The `deal.II` library, version 9.1, *J Numer Math* **27**, accepted.
2. U. M. Ascher, S. J. Ruuth and B. T. R. Wetton, Implicit-explicit methods for time-dependent partial differential equations, *SIAM J Numer Anal* **32** (1995) 797–823.
3. C. M. Augustin, A. Neic, M. Liebmann, A. J. Prassl, S. A. Niederer, G. Haase and G. Plank, Anatomically accurate high resolution modeling of human whole heart electromechanics: A strongly scalable algebraic multigrid solver method for nonlinear deformation, *J Comput Phys* **305** (2016) 622–646.
4. J. D. Bayer, R. C. Blake, G. Plank and N. A. Trayanova, A novel rule-based algorithm for assigning myocardial fiber orientation to computational heart models, *Ann Biomed Eng* **40** (2012) 2243–2254.
5. M. Benzi, G. H. Golub and J. Liesen, Numerical solution of saddle point problems, *Acta Numer* **14** (2005) 1–137.
6. D. M. Bers, Cardiac excitation–contraction coupling, *Nature* **415** (2002) 198–205.
7. P. Blanco and R. Feijòo, A dimensionally-heterogeneous closed-loop model for the cardiovascular system and its applications, *Med Eng Phys* **35** (2013) 652–667.
8. S. Brenner and R. Scott, *The Mathematical Theory of Finite Element Methods* (Springer, 2008).
9. C. Burstedde, L. C. Wilcox and O. Ghattas, p4est: Scalable algorithms for parallel adaptive mesh refinement on forests of octrees, *SIAM J Sci Comput* **33** (2011) 1103–1133.
10. O. Camara, M. Sermesant, P. Lamata, L. Wang, M. Pop, J. Relan, M. D. Craene, H. Delingette, H. Liu, S. Niederer, A. Pashaei, G. Plank, D. Romero, R. Sebastian, K. Wong, H. Zhang, N. Ayache, A. Frangi, P. Shi, N. Smith and G. Wright, Inter-model consistency and complementarity: Learning from ex-vivo imaging and electrophysiological data towards an integrated understanding of cardiac physiology, *Prog Biophys Mol Bio* **107** (2011) 122–133.
11. D. Canuto, K. Chong, C. Bowles, E. P. Dutson, J. D. Eldredge and P. Benharash, A regulated multiscale closed-loop cardiovascular model, with applications to hemorrhage and hypertension, *Int J Numer Meth Bio* **34** (2018) e2975.
12. R. Chabiniok, V. Y. Wang, M. Hadjicharalambous, L. Asner, J. Lee, M. Sermesant, E. Kuhl, A. A. Young, P. Moireau, M. P. Nash, D. Chapelle and D. A. Nordslet-

ten, Multiphysics and multiscale modelling, data–model fusion and integration of organ physiology in the clinic: ventricular cardiac mechanics, *Interface Focus* **6** (2016) 20150083.
13. P. Chinchapatnam, K. S. Rhode, M. Ginks, C. A. Rinaldi, P. Lambiase, R. Razavi, S. Arridge and M. Sermesant, Model-based imaging of cardiac apparent conductivity and local conduction velocity for diagnosis and planning of therapy, *IEEE T Med Imaging* **27** (2008) 1631–1642.
14. F. S. Costabal, D. E. Hurtado and E. Kuhl, Generating purkinje networks in the human heart, *J Biomech* **49** (2016) 2455–2465.
15. S. de Putter, B. Wolters, M. Rutten, M. Breeuwer, F. Gerritsen and F. van de Vosse, Patient-specific initial wall stress in abdominal aortic aneurysms with a backward incremental method, *J Biomech* **40** (2007) 1081–1090.
16. L. Dedè, A. Quarteroni and F. Regazzoni, Mathematical and numerical models for the cardiac electromechanical function, *Atti della Accademia Nazionale dei Lincei, Classe di Scienze Fisiche, Matematiche e Naturali. Rendiconti Lincei - Matematica e Applicazioni* **32** (2021) 233–272.
17. M. Deo, P. Boyle, G. Plank and E. Vigmond, Arrhythmogenic mechanisms of the purkinje system during electric shocks: A modeling study, *Heart Rhythm* **6** (2009) 1782–1789.
18. M. Fedele and A. Quarteroni, Polygonal surface processing and mesh generation tools for the numerical simulation of the cardiac function, *Int J Numer Meth Bio* **37**.
19. P. C. Franzone and L. Guerri, Spreading of excitation in 3-d models of the anisotropic cardiac tissue. i. validation of the eikonal model, *Math Biosci* **113** (1993) 145–209.
20. P. C. Franzone, L. Guerri and S. Rovida, Wavefront propagation in an activation model of the anisotropic cardiac tissue: asymptotic analysis and numerical simulations, *J Math Biol* **28** (1990) 121–176.
21. P. C. Franzone, L. Pavarino and B. Taccardi, Simulating patterns of excitation, repolarization and action potential duration with cardiac bidomain and monodomain models, *Math Biosci* **197** (2005) 35–66.
22. P. C. Franzone, L. F. Pavarino and G. Savaré, Computational electrocardiology: mathematical and numerical modeling, in *Complex Systems in Biomedicine* (Springer Milan, 2006), pp. 187–241.
23. P. C. Franzone, L. F. Pavarino and S. Scacchi, Bioelectrical effects of mechanical feedbacks in a strongly coupled cardiac electro-mechanical model, *Math Mod Meth Appl S* **26** (2015) 27–57.
24. P. C. Franzone, L. F. Pavarino and S. Scacchi, Effects of mechanical feedback on the stability of cardiac scroll waves: A bidomain electro-mechanical simulation study, *Chaos: An Interdisciplinary Journal of Nonlinear Science* **27** (2017) 093905.
25. M. W. Gee, C. Förster and W. A. Wall, A computational strategy for prestressing patient-specific biomechanical problems under finite deformation, *Int J Numer Meth Bio* **26** (2010) 52–72.
26. J. M. Guccione, A. D. McCulloch and L. K. Waldman, Passive material properties of intact ventricular myocardium determined from a cylindrical model, *J Biomech Eng* **113** (1991) 42–55.
27. M. Hirschvogel, M. Bassilious, L. Jagschies, S. M. Wildhirt and M. W. Gee, A monolithic 3d-0d coupled closed-loop model of the heart and the vascular system: Experiment-based parameter estimation for patient-specific cardiac mechanics, *Int J Numer Meth Bio* **33** (2017) e2842.
28. Y. Hu, V. Gurev, J. Constantino, J. D. Bayer and N. A. Trayanova, Effects of mechano-electric feedback on scroll wave stability in human ventricular fibrillation, *Plos ONE*

8 (2013) e60287.
29. J. Hussan, P. P. de Tombe and J. J. Rice, A spatially detailed myofilament model as a basis for large-scale biological simulations, *IBM J Res Dev* **50** (2006) 583–600.
30. Z. M. G. Inc., *The Zygote Solid 3D Heart Model* (2013).
31. R. C. Kerckhoffs, O. P. Faris, P. H. Bovendeerd, F. W. Prinzen, K. Smits, E. R. McVeigh and T. Arts, Timing of depolarization and contraction in the paced canine left ventricle:, *J Cardiovasc Electr* **14** (2003) S188–S195.
32. E. Konukoglu, J. Relan, U. Cilingir, B. H. Menze, P. Chinchapatnam, A. Jadidi, H. Cochet, M. Hocini, H. Delingette, P. Jaïs, M. Haïssaguerre, N. Ayache and M. Sermesant, Efficient probabilistic model personalization integrating uncertainty on data and parameters: Application to eikonal-diffusion models in cardiac electrophysiology, *Prog Biophys Mol Bio* **107** (2011) 134–146.
33. S. Land, S.-J. Park-Holohan, N. P. Smith, C. G. dos Remedios, J. C. Kentish and S. A. Niederer, A model of cardiac contraction based on novel measurements of tension development in human cardiomyocytes, *J Mol Cell Cardiol* **106** (2017) 68–83.
34. A. Maceira, S. Prasad, M. Khan and D. Pennell, Normalized left ventricular systolic and diastolic function by steady state free precession cardiovascular magnetic resonance, *J Cardiov Magn Reson* **8** (2006) 417–426.
35. L. Marx, M. A. F. Gsell, A. Rund, F. Caforio, A. J. Prassl, G. Toth-Gayor, T. Kuehne, C. M. Augustin and G. Plank, Personalization of electro-mechanical models of the pressure-overloaded left ventricle: fitting of windkessel-type afterload models, *Philos T Roy Soc A* **378** (2020) 20190342.
36. M. P. Nash and A. V. Panfilov, Electromechanical model of excitable tissue to study reentrant cardiac arrhythmias, *Prog Biophys Mol Bio* **85** (2004) 501–522.
37. A. Neic, F. O. Campos, A. J. Prassl, S. A. Niederer, M. J. Bishop, E. J. Vigmond and G. Plank, Efficient computation of electrograms and ECGs in human whole heart simulations using a reaction-eikonal model, *J Comput Phys* **346** (2017) 191–211.
38. S. Niederer, P. Hunter and N. Smith, A quantitative analysis of cardiac myocyte relaxation: A simulation study, *Biophys J* **90** (2006) 1697–1722.
39. S. A. Niederer, E. Kerfoot, A. P. Benson, M. O. Bernabeu, O. Bernus, C. Bradley, E. M. Cherry, R. Clayton, F. H. Fenton, A. Garny, E. Heidenreich, S. Land, M. Maleckar, P. Pathmanathan, G. Plank, J. F. Rodriguez, I. Roy, F. B. Sachse, G. Seemann, O. Skavhaug and N. P. Smith, Verification of cardiac tissue electrophysiology simulators using an n -version benchmark, *Philos T R Soc A* **369** (2011) 4331–4351.
40. R. Ogden, ed., *Non-linear elastic deformations* (Dover Publications, 1997).
41. S. Palamara, C. Vergara, E. Faggiano and F. Nobile, An effective algorithm for the generation of patient-specific purkinje networks in computational electrocardiology, *J Comput Phys* **283** (2015) 495–517.
42. M. R. Pfaller, J. M. Hörmann, M. Weigl, A. Nagler, R. Chabiniok, C. Bertoglio and W. A. Wall, The importance of the pericardium for cardiac biomechanics: from physiology to computational modeling, *Biomech Model Mechan* **18** (2018) 503–529.
43. R. Piersanti, P. C. Africa, M. Fedele, C. Vergara, L. Dedè, A. F. Corno and A. Quarteroni, Modeling cardiac muscle fibers in ventricular and atrial electrophysiology simulations, *Comput Method Appl M* **373** (2021) 113468.
44. G. Plank, L. Zhou, J. L. Greenstein, S. Cortassa, R. L. Winslow, B. O'Rourke and N. A. Trayanova, From mitochondrial ion channels to arrhythmias in the heart: computational techniques to bridge the spatio-temporal scales, *Philos T R Soc A* **366** (2008) 3381–3409.
45. M. Potse, B. Dube, J. Richer, A. Vinet and R. Gulrajani, A comparison of mon-

odomain and bidomain reaction-diffusion models for action potential propagation in the human heart, *IEEE T Bio-Med Eng* **53** (2006) 2425–2435.
46. A. Quarteroni, L. Dede', A. Manzoni and C. Vergara, *Mathematical Modelling of the Human Cardiovascular System* (Cambridge University Press, 2019).
47. A. Quarteroni, R. Sacco and F. Saleri, *Numerical Mathematics* (Springer, 2007).
48. A. Quarteroni and A. Valli, *Numerical Approximation of Partial Differential Equations* (Springer Berlin Heidelberg, 1994).
49. F. Regazzoni, L. Dedè and A. Quarteroni, Active contraction of cardiac cells: a reduced model for sarcomere dynamics with cooperative interactions, *Biomech Model Mechan* **17** (2018) 1663–1686.
50. F. Regazzoni, L. Dedè and A. Quarteroni, Biophysically detailed mathematical models of multiscale cardiac active mechanics, *PLOS Comput Biol* **16** (2020) e1008294.
51. F. Regazzoni, L. Dedè and A. Quarteroni, Machine learning of multiscale active force generation models for the efficient simulation of cardiac electromechanics, *Comput Method Appl M* **370** (2020) 113268.
52. F. Regazzoni, L. Dedè and A. Quarteroni, Active force generation in cardiac muscle cells: mathematical modeling and numerical simulation of the actin-myosin interaction, *Vietnam Journal of Mathematics* **49** (2021) 87–118.
53. F. Regazzoni and A. Quarteroni, Accelerating the convergence to a limit cycle in 3d cardiac electromechanical simulations through a data-driven 0d emulator, *Computers in Biology and Medicine* **135** (2021) 104641.
54. F. Regazzoni, M. Salvador, P. Africa, M. Fedele, L. Dedè and A. Quarteroni, A cardiac electromechanical model coupled with a lumped-parameter model for closed-loop blood circulation, *Journal of Computational Physics* **457** (2022) 111083.
55. S. Rossi, Anisotropic modeling of cardiac mechanical activation, Ph.D. thesis, EPFL, 2014.
56. Y. Saad and M. H. Schultz, GMRES: A generalized minimal residual algorithm for solving nonsymmetric linear systems, *SIAM J Sci Stat Comp* **7** (1986) 856–869.
57. J. Sainte-Marie, D. Chapelle, R. Cimrman and M. Sorine, Modeling and estimation of the cardiac electromechanical activity, *Comput Struct* **84** (2006) 1743–1759.
58. M. Salvador, L. Dede' and A. Quarteroni, An intergrid transfer operator using radial basis functions with application to cardiac electromechanics, *Comput Mech* **66** (2020) 491–511.
59. R. Sebastian, S. Ordas, G. Plank, B. Rodriguez, E. J. Vigmond and A. F. Frangi, Assessing influence of conductivity in heart modelling with the aim of studying cardiovascular diseases, in *Medical Imaging 2008: Physiology, Function, and Structure from Medical Images*, eds. X. P. Hu and A. V. Clough (SPIE, 2008).
60. N. P. Smith, D. P. Nickerson, E. J. Crampin and P. J. Hunter, Multiscale computational modelling of the heart, in *Acta Numerica 2004* (Cambridge University Press, 2004), pp. 371–431.
61. M. Strocchi, C. M. Augustin, M. A. F. Gsell, E. Karabelas, A. Neic, K. Gillette, O. Razeghi, A. J. Prassl, E. J. Vigmond, J. M. Behar, J. Gould, B. Sidhu, C. A. Rinaldi, M. J. Bishop, G. Plank and S. A. Niederer, A publicly available virtual cohort of four-chamber heart meshes for cardiac electro-mechanics simulations, *PLOS ONE* **15** (2020) e0235145.
62. M. Strocchi, M. A. Gsell, C. M. Augustin, O. Razeghi, C. H. Roney, A. J. Prassl, E. J. Vigmond, J. M. Behar, J. S. Gould, C. A. Rinaldi, M. J. Bishop, G. Plank and S. A. Niederer, Simulating ventricular systolic motion in a four-chamber heart model with spatially varying robin boundary conditions to model the effect of the pericardium, *J Biomech* **101** (2020) 109645.

63. K. H. W. J. ten Tusscher and A. V. Panfilov, Alternans and spiral breakup in a human ventricular tissue model, *Am J Physiol-Heart C* **291** (2006) H1088–H1100.
64. N. Trayanova, Defibrillation of the heart: insights into mechanisms from modelling studies, *Exp Physiol* **91** (2006) 323–337.
65. C. Vergara, M. Lange, S. Palamara, T. Lassila, A. F. Frangi and A. Quarteroni, A coupled 3d–1d numerical monodomain solver for cardiac electrical activation in the myocardium with detailed purkinje network, *J Comput Phys* **308** (2016) 218–238.
66. C. Vergara, S. Palamara, D. Catanzariti, F. Nobile, E. Faggiano, C. Pangrazzi, M. Centonze, M. Maines, A. Quarteroni and G. Vergara, Patient-specific generation of the purkinje network driven by clinical measurements of a normal propagation, *Med Biol Eng Comput* **52** (2014) 813–826.
67. E. J. Vigmond and B. D. Stuyvers, Modeling our understanding of the his-purkinje system, *Prog Biophys Mol Bio* **120** (2016) 179–188.
68. T. Washio, J. ichi Okada, A. Takahashi, K. Yoneda, Y. Kadooka, S. Sugiura and T. Hisada, Multiscale heart simulation with cooperative stochastic cross-bridge dynamics and cellular structures, *Multiscale Model Sim* **11** (2013) 965–999.
69. N. Westerhof, J.-W. Lankhaar and B. E. Westerhof, The arterial windkessel, *Med Biol Eng* **47** (2008) 131–141.